Astronomy & Astrophysics

HERMES: Gamma-ray burst and gravitational wave counterpart hunter[*]

G. Ghirlanda[1,2,**], L. Nava[1], O. Salafia[1,2], F. Fiore[3,4], R. Campana[5,6], R. Salvaterra[7], A. Sanna[8],
W. Leone[9], Y. Evangelista[10,11], G. Dilillo[10], S. Puccetti[12], A. Santangelo[13], M. Trenti[14,15], A. Guzmán[13],
P. Hedderman[13], G. Amelino-Camelia[16], M. Barbera[23], G. Baroni[3], M. Bechini[17], P. Bellutti[18], G. Bertuccio[19],
G. Borghi[18], A. Brandonisio[17], L. Burderi[8], C. Cabras[20], T. Chen[21], M. Citossi[3], A. Colagrossi[17], R. Crupi[29],
F. De Cecio[17], I. Dedolli[19], M. Del Santo[22], E. Demenev[18], T. Di Salvo[23], F. Ficorella[18], D. Gačnik[24],
M. Gandola[19], N. Gao[21], A. Gomboc[25], M. Grassi[26], R. Iaria[23], G. La Rosa[22], U. Lo Cicero[30], P. Malcovati[26],
A. Manca[8], E. J. Marchesini[5], A. Maselli[28], F. Mele[19], P. Nogara[22], G. Pepponi[18], M. Perri[28], A. Picciotto[18],
S. Pirrotta[12], J. Prinetto[17], M. Quirino[17], A. Riggio[8], J. Řípa[27], F. Russo[22], D. Selčan[24], S. Silvestrini[17],
G. Sottile[22], M. L. Thomas[14], A. Tiberia[12], S. Trevisan[3], I. Troisi[17], A. Tsvetkova[8,5], A. Vacchi[29],
N. Werner[27], G. Zanotti[17], and N. Zorzi[18]

(Affiliations can be found after the references)

ABSTRACT

Gamma-ray bursts (GRBs) bridge relativistic astrophysics and multimessenger astronomy. Space–based γ- and X-ray wide-field detectors have proven essential for detecting and localizing the highly variable GRB prompt emission, which is also a counterpart of gravitational wave events. We studied the capability of detecting long and short GRBs with the High Energy Rapid Modular Ensemble of Satellites (HERMES) Pathfinder (HP) and SpIRIT, namely a swarm of six 3U CubeSats to be launched in early 2025, and a 6U CubeSat launched on December 1 2023. We also studied the capabilities of two advanced configurations of swarms of more than eight satellites with improved detector performances (HERMES Constellations). The HERMES detectors, sensitive down to ∼2–3 keV, will be able to detect faint and soft GRBs, which comprise X-ray flashes and high-redshift bursts. By combining state-of-the-art long- and short-GRB population models with a description of the single module performance, we estimate that HP will detect ∼195$^{+22}_{-21}$ long GRBs (3.4$^{+0.3}_{-0.8}$ at redshift $z > 6$) and ∼19$^{+5}_{-3}$ short GRBs per year. The larger HERMES Constellations under study can detect between ∼1300 and ∼3000 long GRBs per year and between ∼160 and ∼400 short GRBs per year, depending on the chosen configuration, with a rate of long GRBs above $z > 6$ of between 30 and 75 per year. Finally, we explored the capability of HERMES to detect short GRBs as electromagnetic counterparts of binary neutron star (BNS) mergers detected as gravitational signals by current and future ground–based interferometers. Under the assumption that the GRB jets are structured, we estimate that HP can provide up to ∼1 (14) yr^{-1} joint detections during the fifth LIGO–Virgo–KAGRA observing run (*Einstein* Telescope single triangle 10 km arm configuration). These numbers become ∼4 (100) yr^{-1}, respectively, for the HERMES Constellation configuration.

Key words. gravitational waves – space vehicles: instruments – gamma-ray burst: general

1. Introduction

Gamma-ray bursts (GRBs) release a large amount of electromagnetic energy ($E_\gamma \sim 10^{51}$ erg) over a short timescale ($\sim 10^{-2}$–10^3 seconds) as a result of energy dissipation in a strongly collimated (a few degrees in width) jet, in which particles move at ultrarelativistic velocities ($\Gamma \gtrsim 100$). The initial radiative phase (i.e., the "prompt emission") is detected in the keV–MeV range. The flux variability timescale during this phase can be as short as 1–10 ms (MacLachlan et al. 2013; Golkhou et al. 2015). The origin of this fast variability, its connection to the central engine and to the properties of the region where the radiation is produced, and the origin of the radiation itself are still largely unknown.

Traditionally, GRBs have been categorized into "long" and "short" bursts based on their observed prompt emission duration, with a separation[1] at 2 seconds (Kouveliotou et al. 1993). Direct (imaging) and indirect (light-curve photometry and spectroscopy) detections of long-GRB–supernova associations have now been used to establish that many long-duration GRBs originate from the core collapse of massive stars (Levan et al. 2016), as originally hypothesized by Woosley (1993). The first conclusive evidence linking short-duration GRBs to the merger of compact object binaries including at least one neutron star (NS), as initially proposed by Eichler et al. (1989) and Narayan et al. (1992), came from the association of GRB170817A (Abbott et al. 2017a) and the kilonova AT2017gfo (Coulter et al. 2017; Pian et al. 2017) with the first gravitational wave (GW) signal from the merger of two NSs (Abbott et al. 2017b) detected by the Advanced Laser Interferometer Gravitational wave Observatory

---

[1] The most recent results show that the separation in observer frame duration does not map the two progenitor channels exactly; see e.g., GRB 211211A (Rastinejad et al. 2022) and GRB 200826A (Bromberg et al. 2013; Rossi et al. 2022).

(aLIGO, LIGO Scientific Collaboration 2015) and Advanced Virgo (Acernese et al. 2015).

The detection rates of compact binary mergers will increase in the next decade thanks to joint observation runs of the Advanced Virgo, aLIGO, and KAGRA (Akutsu et al. 2020). Predictions of the joint electromagnetic (EM) and GW detections are currently under development (see e.g. Colombo et al. 2022, 2024). A major step forward in the detection capabilities of GWs will be achieved with third-generation interferometers, such as the *Einstein* Telescope (ET; Punturo et al. 2010; Maggiore et al. 2020; Branchesi et al. 2023) and the Cosmic Explorer (CE; Abbott et al. 2017a; Reitze et al. 2019), which will enable the discovery and follow-up of hundreds of EM counterparts (see e.g., Ronchini et al. 2022).

The GRB prompt emission is followed by a longer-lasting afterglow emission produced by the interaction of the jet with the external medium. This component is typically detected in the X-rays and optical bands and, less often, in the radio and in the GeV gamma rays. Since 2018, five GRB afterglows have been firmly detected at very-high energy (VHE, >100 GeV) as well (for a recent review, see Miceli & Nava 2022). Photons with energies of up to ~10 TeV have been detected by LHAASO from GRB 221009A (Huang et al. 2022), the brightest GRB ever detected. There is general consensus over the identification of the origin of this emission as the synchrotron self-Compton component (MAGIC Collaboration 2019; Salafia et al. 2022), although other possibilities are being investigated (H.E.S.S. Collaboration 2021). The detections at VHE are still very limited and sparse, and a full exploitation of VHE observations will be achieved (Bernardini et al. 2019) only with the advent of the Cherenkov Telescope Array (CTA), the next generation of imaging atmospheric Cherenkov telescopes (IACTs); the full array is expected to be operational from 2025. Similarly, at the opposing extreme, in the radio band, the follow up and imaging of GRB jets have provided a unique opportunity to explore the jet (e.g., Mooley et al. 2018; Ghirlanda et al. 2019) and the properties of the ambient medium (e.g., Salafia & Ghirlanda 2022; Giarratana et al. 2022). The current limited number of radio-detected GRBs (Chandra & Frail 2012) should increase with the advent of the Square Kilometer Array (SKA) and its pathfinders (Ghirlanda et al. 2013, 2014).

The lessons learned over the past 50 years, since the discovery of GRBs, underscore that almost all the GRB-related science, including the recent multimessenger (MM) advancements, is enabled by the detection and localization of the GRB prompt event. Currently, the most active space telescopes for the search and study of GRBs are the *Neil Gehrels Swift* Observatory (Gehrels et al. 2004) and the *Fermi* satellite (Meegan et al. 2009), which have now been operational for 19 and 15 years, respectively. Together, these detect about 300 GRBs per year. The continuation of their activity after 2024 is not guaranteed. *Swift*/BAT (15–350 keV) provides good GRB localizations (several arcminutes) enabling rapid follow up in other bands, eventually leading (in about 30% of events) to the determination of the redshift of the GRB. On the other hand, *Fermi* (8 keV–100 GeV), while providing less precise localizations (to within several degrees), allows the study of the temporal and spectral variability of prompt emission across nearly seven orders of magnitude in energy.

In order to maximize the impact that major future facilities, such as CTA and SKA, and next-generation gravitational wave interferometers may have in the GRB field and fields related to multimessenger astronomy, a facility is needed to search for GRBs and provide accurate localizations and temporal/spectral information.

At the present stage, the Space Variable Objects Monitor (SVOM, Atteia et al. 2022) is planned to become operative by the end of 2024, and the Einstein Probe satellite (EP, Yuan et al. 2022) was successfully launched on January 2024. The SVOM estimated rate of alerts, with localization capabilities similar to BAT, is 50–60 GRB yr^{-1}, while for an additional 90 GRBs the localization is expected to be $\lesssim 5-10$ degrees. EP can provide several GRB detections with accurate localizations for multiband follow up of their afterglow emission. However, its limited energy range (0.3–5 keV for the Wide X-ray Telescope, and extended up to 10 keV by the narrow-field Follow up X-ray Telescope) prevents a detailed spectral characterization of the prompt GRB emission as currently possible with *Fermi* for example.

Mission concepts such as the Transient High-Energy Sky and Early Universe Surveyor (THESEUS, Amati et al. 2021) and the Gamow Explorer (White et al. 2021) are being developed. THESEUS, comprising a suite of instruments sensitive in the keV–MeV energy range with imaging capabilities at the lower end of this range, will detect hundreds of GRBs per year, with a considerable fraction detected at high redshifts. The fast repointing capabilities and the presence of an infrared telescope on board will secure a factor-ten increase in the number of GRBs with measured distance at $z \geq 6$, which is presently eight (Amati et al. 2021).

Given this status of the field, it would be highly beneficial to complement existing and planned observatories with a technology that can be built on short timescales (a few years) and at an affordable cost (Fiore et al. 2021). The High-Energy Rapid Modular Ensemble of Satellites (HERMES) discussed in this paper is designed to serve this purpose. GRB monitoring by CubeSats has been successfully demonstrated by for example GRBalpha (Pál et al. 2020, 2023; Řípa et al. 2022) and VZLUSAT-2 (Granja et al. 2022), which have detected ~60 and ~30 GRBs up to February 2024, respectively. GRBAlpha is a 1U CubeSat launched on March 22 2021 on a low Earth–Sun synchronous orbit (SSO). It hosts a CsI(Tl) scintillator crystal read out by an array of silicon photo multipliers, providing a peak collecting area of ~50 cm^2 in the 70–800 keV energy band. VZLUSAT-2 was launched in an SSO on January 13, 2022, and hosts two gamma-ray detectors similar to that on board GRBAlpha. GRBAlpha and VZLUSAT-2 are finishing or surpassing their third and second year in orbit, showing the sustained in-orbit reliability achieved by CubeSats and instruments for high-energy astrophysics.

In this paper, we calculate the detection rates of short and long GRBs with HERMES. We derive the characteristics of GRBs that can be detected by HERMES and compare them with existing datasets of GRBs detected by *Swift*/BAT and *Fermi*/GBM. Additionally, we assess the rate of joint detection of short GRBs by HERMES and GWs from binary NS mergers by aLIGO and Advanced Virgo in O5, and by ET at design sensitivity.

The paper is organized as follows. Section 2 introduces the HERMES mission. In Sect. 3, we describe how we evaluate the capabilities of HERMES in detecting both short and long GRBs. Section 4 focuses on the joint EM-GW detections with ET. We provide a discussion and summary of our findings in Sect. 5. Throughout the paper, we adopt a standard flat cosmology with $\Omega_M = 0.3, h = 0.7$.

2. The HERMES mission

HERMES[2] is a modular X-ray space mission specifically dedicated to the study of GRBs and fast X-ray transients. To

---

demonstrate its capabilities, three technological (HERMES-TP, funded by the Italian Space Agency (ASI)) and three scientific (HERMES-SP, funded by the European Commission Horizon 2020 Research and Innovation Program) pathfinder units are in preparation. Together, these constitute the HERMES Pathfinder (HP hereafter). The primary goals of the HP are the validation of the capability to detect GRBs and other fast transients with miniaturized instrumentation hosted by CubeSats and to obtain their localization using the triangulation technique (Thomas et al. 2023), which measures the arrival time delay of the signal across different detectors located thousands of kilometres apart (Fiore et al. 2020, 2022).

The HERMES Pathfinder is composed of six units – each measuring $10 \times 10 \times 30$ cm for a total weight of 6 kg – classified as 3U CubeSats. These units are scheduled for launch in early 2025. Additionally, a seventh instrument payload, identical to those used in HP, is hosted by the SpIRIT (Space Industry Responsive Intelligent Thermal nanosatellite[3]) CubeSat, which was deployed by the University of Melbourne (Trenti 2021). SpIRIT, a 6U CubeSat, was launched into SSO on December 1, 2023. It is currently in a commissioning phase and scientific observations are expected to start in the second quarter of 2024. So far, its performance appears nominal. This crucial experiment is validating the instrument design, which was entirely realized by Istituto Nazionale di Astrofisica (INAF) and its partner Politecnico di Milano. The approach chosen for the development of the instrument is based on the design and realization of critical subsystems, such as the silicon drift detectors (SDDs) and the on board software, on the basis of scientific agreements with the providers Fondazione Bruno Kessler and the University of Tubingen, and the use of commercial off-the-shelf (COTS) components. SpIRIT will also be crucial for testing the HP payload in the harsh space environment and in different thermal conditions. The SDDs employed by the HP payload suffer damage due to energetic particles, such as electrons and protons. SpIRIT will allow us to quantify for the first time the degradation of SDD performance in SSO. The SDD noise properties also depend on the operating temperature, and improve toward lower temperatures. Among the SpIRIT payloads, there is also an active temperature control system based on a Stirling cycle cryocooler and deployable thermal radiators (the TheMIS payload). We therefore will test the performances of the HP payload in a wide temperature range, from $-30\,°C$ (the operational limit of the HERMES payload) to $+20\,°C$, allowing us to identify the optimal temperature range for using the instrument, and therefore the requirements for the thermal control system in view of the application on the HERMES Constellation.

Therefore, the HERMES Pathfinder in conjunction with SpIRIT will consists of seven satellites on two different orbital planes. SpIRIT and HERMES Pathfinder serve as a test for the project of the a larger constellation comprising tens of CubeSat modules (HERMES Constellation, hereafter).

HERMES Pathfinder and SpIRIT host simple but innovative X-ray detectors, characterized by a particularly wide energy band, from 2–3 keV to ~2 MeV, and an excellent temporal resolution of about 300 ns, which is three to seven times higher than the best resolution achieved so far for GRB studies. Each CubeSat hosts a detector (see e.g., Evangelista et al. 2020, 2022) that is sensitive to both X-rays (X-mode or simply X, hereafter) and soft γ-rays (S-mode or S, hereafter). The X/Gamma ray Imaging Spectrometer (XGIS) instrument on board THESEUS (Amati et al. 2021) is based on the same "siswich" architecture.

The characteristics of each HP unit are listed in the first row of Table 1. The effective area as a function of photon energy is shown in Fig. 1 for different values of the boresight angle θ between the source direction and the detector normal (see Campana et al. 2020, 2022 for more details). The shaded regions in Fig. 1 show the energy ranges (also reported in Table 1) used for the computation of the detection rate (Sect. 2). The effective area of the detector decreases with increasing boresight angle, especially for the lower photon energies for which we plot only the effective area up to 60 degrees. The effective areas shown in Fig. 1 were computed by means of Geant4-based Monte Carlo simulations (Agostinelli et al. 2003) using an updated satellite mass model (much more accurate than the simplified version discussed in Campana et al. 2020). The mass model includes a detailed geometrical and physical description of the detector and of the main components of the spacecraft avionics. For simplicity, the small dependence for fixed θ values over the azimuth angle has been here averaged out. Moreover, the background count rates reported in Table 1 were estimated by simulating all the various expected contributions in LEO (e.g., CXB, cosmic rays, Earth albedo, etc; see Campana et al. 2013 for more details on the assumed models). The HERMES orbital configuration implies that the satellites be released in very close orbits, which nevertheless guarantees a natural drift along the velocity-bar direction to achieve the baseline distance between the elements of the constellation (Colagrossi et al. 2020). The HERMES natural dynamics evolves in a periodic motion of about 80–100 d, and the pointing direction of each spacecraft will be controlled and optimized to cope with this dynamical evolution [2]. Then, to maintain the overlapping field of view (FoV) of at least three spacecraft, and to maximize the sky coverage, the spacecraft will follow an optimized pointing strategy according to dedicated pointing optimization software (Colagrossi et al. 2020, 2019).

The full HERMES Constellation is based on the HP concept, but is designed to carry detectors of superior sensitivity. Here, we present a preparatory study, investigating two different configurations for the detectors on board the full constellation. In particular, we consider detectors with a larger (by a factor of 4) effective area than HP and a FoV similar to that of the HP (Constellation A) or smaller by a factor 2 (Constellation B). The latter assumption of a smaller FoV ensures that Constellation B has a lower X-ray background rate than Constellation A. The properties of a single unit for Constellations A and B are listed in Table 1. For the configuration called Constellation A, we assume 9 CubeSats simultaneously in orbit, while for Constellation B we assume 13 CubeSats to compensate for their smaller FoV and to assure full sky coverage. The sky coverage maps (Fig. 2) show, for each location in the sky, the minimum boresight angle among all the detectors observing that location.

3. GRB detection rates

We employed a population-synthesis approach to assess the GRB detection capabilities of HERMES. This involves creating a realistic mock population of GRBs through Monte Carlo simulations. For each simulated GRB, we calculated the likelihood of it being detected by HERMES, taking into account the instrumental characteristics outlined in Table 1 and illustrated in Fig. 1. This allows a more detailed analysis of the instrumental performance, such as the boresight-angle dependence of the effective area (Fig. 1) and the sky coverage of a swarm of satellites (Fig. 2), in addition to the simple scaling of factors like the FoV and the duty cycle.

Table 1. Characteristics describing one single HERMES module.

	Detection mode	FoV sr	Energy range keV	Back. rate counts/s	Effective area
HP	X	3.14	3–20	352	Nominal (Fig. 1)
	S	5.20	50–500	80	Nominal (Fig. 1)
Const. A	X	3.14	3–20	1408	Nominal × 4
	S	5.20	50–500	320	Nominal × 4
Const. B	X	1.57	3–20	704	Nominal × 4
	S	2.60	50–500	160	Nominal × 4

Notes. For the HP module and the two different configurations of the Constellation (A and B) and for each detection mode (X and S), the table reports the FoV of a single unit, defined as the field corresponding to 20% of the on-axis collecting area at 100 keV, the energy range considered for the computation of GRB detection rates, the expected background count rate in the same energy range, and the effective area. For the expected background and the effective areas, see also Campana et al. (2020, 2022).
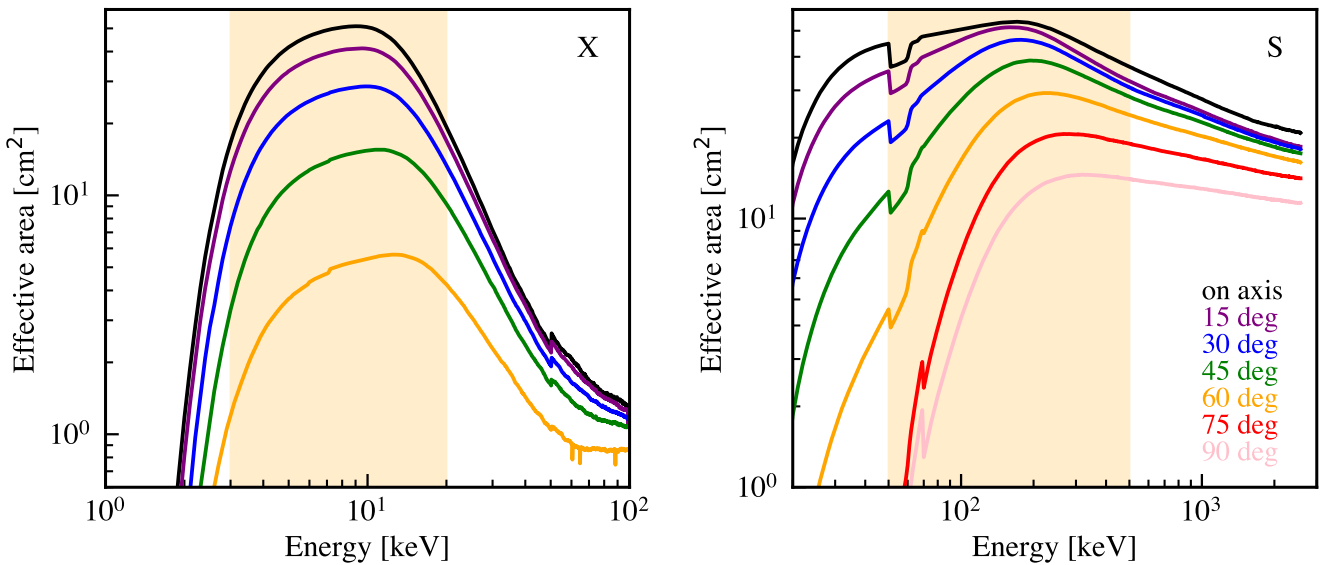

Fig. 1. Effective areas of the X-mode (left-hand panel) and the S-mode (right-hand panel) for the HERMES Pathfinder. Differently colored lines show the effective areas as a function of the boresight angle (as reported in the legend). For the X-mode at angles larger than 60 degrees, the effective area is substantially degraded and is not shown for clarity. Shaded vertical stripes show the energy ranges considered in this study to estimate the detection rates. The full HERMES Constellation is assumed to host detectors with a four-times-larger effective area.

We adopt state-of-the-art population models to describe short and long GRBs. The reliability of the population model is ensured by its calibration with actual GRB datasets (e.g., the GRBs detected by *Fermi* and *Swift*). For long GRBs, our model is based on the work of Ghirlanda et al. (2015). For short GRBs, we employ the most recent model developed by Salafia et al. (2023). This model provides a comprehensive description of the short-GRB population within the framework of a quasi-universal structured-jet scenario, as motivated by the expectations that a jet should have an angular structure, and corroborated by the modeling of the multiwavelength afterglow observations of GRB 170817A (see e.g., Salafia & Ghirlanda 2022, and references therein).

3.1. Detection probability estimate

For HP and SpIRIT, we first considered one single module and assigned to each mock GRB an angle θ with respect to the detector normal by distributing the GRBs isotropically in the sky. For the X detector, the effective area becomes negligible for boresight angles of $\theta \gtrsim 60°$ so that any mock GRB located at large angles is considered undetected by the X-mode. Despite the fact

that the effective area of the S-mode is not particularly small at 90 degrees, we consider that possible effects such as the absorption of X-ray photons by the Earth's atmosphere may limit the FoV of the S-mode to $\theta < 80°$. For Constellation A and B, we use the orbital sky coverage maps (Fig. 2) to identify the minimum boresight angle among the detectors for each mock GRB.

We estimated the source photon counts in the detector over a given energy range $E_1 - E_2$ by integrating the source spectrum $N(E) = dN/dA\,dE$ multiplied by the effective area $A_{\rm eff}(E, \theta)$ estimated at the angle θ:

$$S(\theta) = \int_{E_1}^{E_2} N(E)A(E, \theta)dE,\qquad(1)$$

where $N(E)$ is the observer-frame photon spectrum integrated over a given time bin Δt. The integral in Eq. (1) was performed over the 3–20 keV energy range for the X-mode (shaded vertical stripe in Fig. 1, left panel) and 50–500 keV for the S-mode (shaded vertical stripe in Fig. 1, right panel). The expected average background count rates (counts/s) over the same energy ranges are given in Table 1 (Campana et al. 2020). The total background counts $\mathcal{B}$ were then obtained by multiplying the

background count rate by the same duration Δt over which the source spectrum has been accumulated.

The detection probability is determined by the comparison between the number of expected background counts $\mathcal{B}$ and the measured counts C (which we set, for simplicity and given the small Poisson scatter, to the floor of the sum of the expected source counts $\mathcal{S}$ and background counts $\mathcal{B}$). We consider a GRB as detected if the probability associated with measuring at least C counts when the expected counts are $\mathcal{B}$ corresponds to detection at more than 5σ, that is

$$P_{\text{det}} = \sum_{\mathcal{N}=C}^{\infty} p(\mathcal{N}|\mathcal{B}) = 1 - \sum_{\mathcal{N}=0}^{C-1} p(\mathcal{N}|\mathcal{B}) \leq 2.9 \times 10^{-7}, \quad (2)$$

where

$$p(\mathcal{N}|\mathcal{B}) = \frac{\mathcal{B}^{\mathcal{N}} \exp(-\mathcal{B})}{\mathcal{N}!}. \quad (3)$$

While the HERMES trigger algorithms under study will benefit from new approaches (see Dilillo et al. 2024; Ward et al. 2023 and Crupi et al. 2023), a typical generic trigger algorithm is based on the continuous search for a significant increase in the count rate with respect to the average background counts. The current HERMES algorithm is similar to this latter case, because it uses a Bayesian approach that considers the combined likelihood of signals in the detector to send out an alert regarding potential transients or GRBs (Guzman et al. 2020; Bélanger 2013). Without entering into the details, which include a consideration of the light curve shape (e.g., Lien et al. 2014), we consider two extreme trigger criteria, one based on the peak flux and the other one based on the fluence.

For the trigger criterium based on the fluence, the source counts $\mathcal{S}$ are estimated by considering the total emission over the burst duration $\Delta t = T_{\text{dur}}$. The latter is computed for long GRBs as $\Delta t \sim (1 + z)E_{\text{iso}}/L_{\text{iso}}$, while for short GRBs, we assign the durations randomly from a log-normal distribution centered at 0.3 seconds with a dispersion of 0.2 dex. The background counts are estimated by multiplying the average background count rate by the same duration T_{dur}. If the burst duration is longer than 128 s, the fluence for the trigger condition is accumulated only up to 128 s to mimic the anticipated trigger algorithms that could be implemented for HERMES.

For the trigger criterium based on the peak flux, the source counts are obtained by multiplying the GRB peak flux by the duration over which the peak flux has been estimated. For long GRBs, the duration is $\Delta t = 1$ s, that is, we assume that the peak flux is representative of the average flux in the brightest 1 s time bin. For short GRBs, peak fluxes are estimated on a time bin of 64 ms. In both cases, if the time bin is longer than the burst duration, only the trigger criterium based on the fluence is considered. The background counts are estimated by multiplying the background count rate (in counts s^{-1}, see Table 1) by the same duration interval Δt.

3.2. Results

We applied the above methods to the HP and to Constellations A and B. As summarized in Table 1, the Constellation detectors have a four-times-larger effective area than HP. The difference between configurations A and B of the Constellation is related to the single-detector FoV, which is equal to that of the HP single module for Constellation A and is a factor of 2 smaller for Constellation B (Table 1). The reason for considering a smaller

FoV is to limit the X-ray background, which is dominated by the cosmic X-ray background and is approximately proportional to the instrument FoV.

For the HP, we first estimated the detection rate of one single satellite, assuming a duty cycle of 50%. This is a conservative assumption, and a larger duty cycle is expected in the case of an equatorial orbit. We then multiplied the detection rate by a factor of 2, assuming that the six satellites are composed of two triplets, each observing a different region of the sky. In other words, each group of three satellites covers a FoV of ~5.20 sr (with the S-mode instrument) and ~3.14 sr (with the X-mode instrument).

For Constellations A and B, we provide the detection rate assuming the simultaneous use of a sufficient number of satellites pointing in different directions and covering the full sky. The larger the number of satellites in the constellation, the larger the overlap of their FoVs (each satellite of the constellation has a FoV as reported in Table 1). We assume a total of 9 units for Constellation A and 13 for Constellation B. The coverage maps for the two configurations are shown in Fig. 2. The all-sky coverage contributes, together with the increased sensitivity of the single module (owing to the larger effective area), to the increase in the detection rates by the constellation configurations.

We consider a GRB as detected by HERMES if observed in at least one of the two detection modes (X or S) and by at least one of the two trigger algorithms (peak flux or fluence). In order to derive the detection rates and their associated uncertainties, we simulated 500 long- and 500 short-GRB populations by sampling the posterior distributions of the parameters defining the populations. We estimated the detection rates for every single realization of the population and derived, as final detection rates, the 50th percentile of the distribution of the 500 rate values. Uncertainties at the 68% credible interval were estimated by taking the 16th and the 84th percentiles. The inferred rates and their uncertainties[4] are reported in Table 2. The table shows, both for short and long GRBs, the total rate (number of detected GRBs per year) and also partial rates: all the GRBs detected by S, by X, and by X only.

We estimate that HP should detect short GRBs at a rate of ~19^{+5}_{-3} yr^{-1}. All these are detected by the S instrument owing to the harder spectrum of short GRBs (Ghirlanda et al. 2004, 2009). Compared to *Fermi*-GBM (~40 short GRBs yr^{-1}, Poolakkil et al. 2021), the smaller detection rate of HP is due to its smaller effective area. HP should detect long GRBs at a rate of ~195^{+22}_{-21} yr^{-1}. About 26% are detected thanks to the extension of the sensitivity to the soft X-ray energy range (3–20 keV) through the X-mode (see Fig. 3). The latter, owing to the possible implementation of trigger algorithms based on the burst fluence, makes HP competitive with *Fermi*/GBM, which detects long GRBs at a rate of 200 yr^{-1} on average (Poolakkil et al. 2021).

We estimate the possible long- and short-GRB trigger rates with SpIRIT by assuming a scaling factor of 3/4 for the effective area with respect to that assumed for HP and a background count rate scaled for the same factor. This scaling factor is due to the instrument being delivered with one of the four quadrants being nonfunctional. We also consider a 50% observation efficiency given the SSO orbit. We find that SpIRIT could detect 84 (8) long (short) GRBs per year.

Concerning Constellation A, we estimate detection rates of ~1565^{+292}_{-244} long and ~191^{+40}_{-28} short GRBs per year. For Constel-

---

[4] We note that as these rates are estimated independently as the 50th percentile of the distribution of 500 rate values, the total values reported in Table 2 are not strictly the sum of Columns 3 and 4.
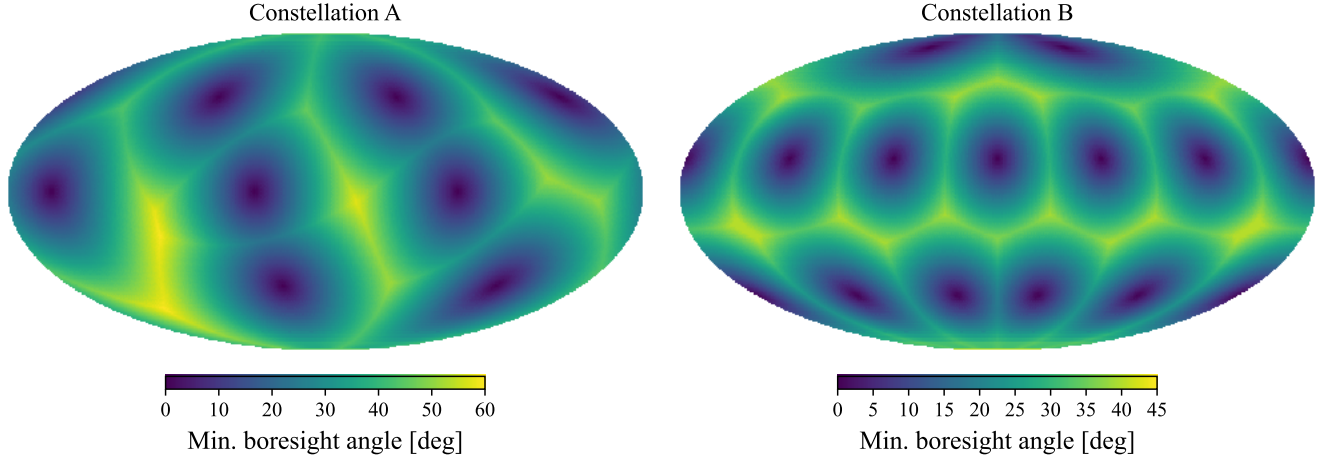
Constellation A

Constellation B

Min. boresight angle [deg]

Min. boresight angle [deg]

Fig. 2. Maps showing the minimum angle between the detector normal and the GRB location for a constellation of 9 CubeSats (Constellation A; left) and a constellation of 13 CubeSats (Constellation B; right).

Table 2. GRB detection rates.

	LONG				SHORT			
	Total	S	X	X-only	Total	S	X	X-only
HP	195^{+22}_{-21}	147^{+13}_{-11}	131^{+17}_{-19}	51^{+12}_{-13}	19^{+5}_{-3}	19^{+5}_{-3}	$0.3^{+0.4}_{-0.2}$	<0.1
Const. A	1565^{+292}_{-244}	772^{+67}_{-61}	1517^{+289}_{-251}	796^{+221}_{-204}	191^{+40}_{-28}	188^{+38}_{-28}	7^{+5}_{-4}	<3
Const. B	2468^{+531}_{-452}	996^{+119}_{-64}	2455^{+529}_{-460}	1473^{+419}_{-375}	327^{+78}_{-61}	322^{+76}_{-58}	18^{+8}_{-10}	<7

Notes. Number of events per year expected with HERMES (HP and Constellation) for the short and long classes. For each GRB class, the table reports the total rate and the partial rates on the single instruments (S – all events detected by S; X – all events detected by X; X-only – all events detected only by the X instrument). The difference in configurations A and B for the Constellation is the FoV of the single satellite (see Table 1).
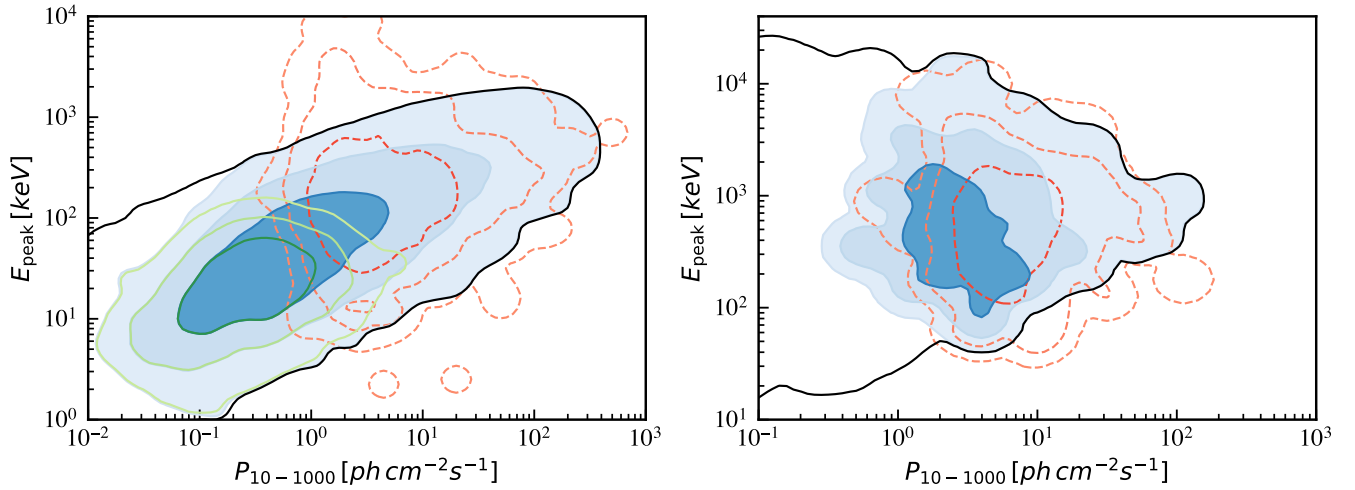

Fig. 3. Distribution of the GRB detected by HERMES (for the case of Constellation B, blue contours) in the plane E_{peak}–peak flux (10–1000 keV) compared with the distribution of real Fermi/GBM GRBs (red dashed contours). Contour levels show the regions containing 68%, 95%, and 99% of the GRBs. Green contours show the HERMES GRBs detected only by the X mode. The black contour refers to the whole simulated population. Left: Long GRB. Right: Short GRBs.

lation B, we find rates of about 2468^{+531}_{-452} long GRBs and 327^{+78}_{-61} short GRBs per year.

Finally, our results show that constellations A and B could detect ~38 and ~70 long GRBs per year at $z > 6$, mainly thanks to the X-mode low-energy extension. Already with HERMES Pathfinder, we estimate that ~3.4 GRBs at $z > 6$ should be detected every year.

The cumulative detection rates and their 68% credible interval as a function of the photon peak flux and fluence (both integrated into the 10–1000 keV energy range) are shown in Figs. 4 and 5, respectively. As expected, a GRB with large fluence or falling within the FoV of both X and S (i.e., if at an angle of $\theta < 60°$) is detected by both modes. The larger detection rate of the S-mode apparent at large flux and fluence is entirely due
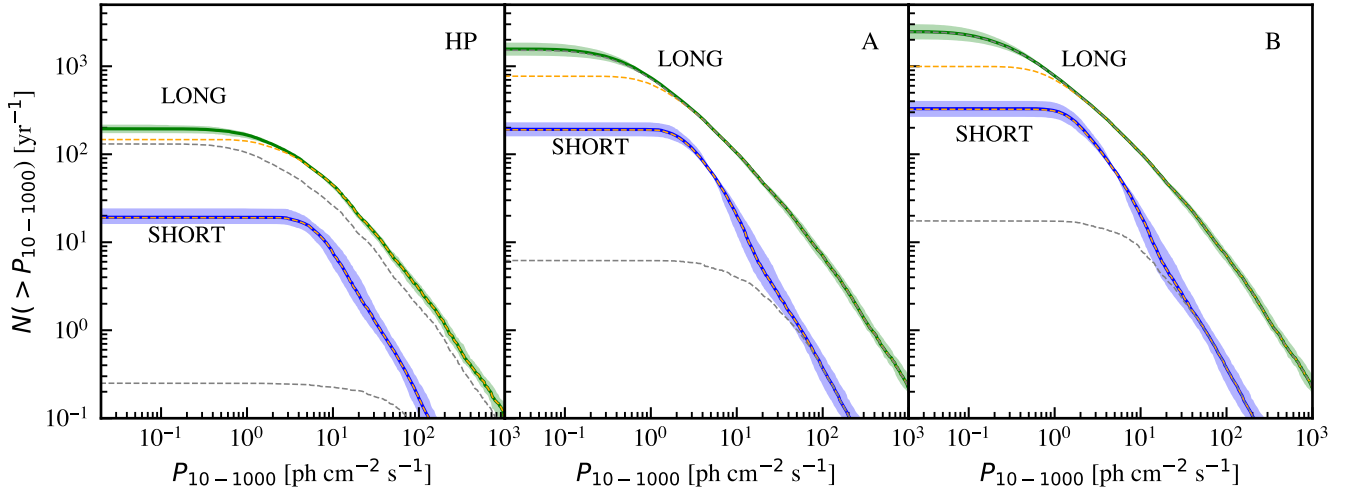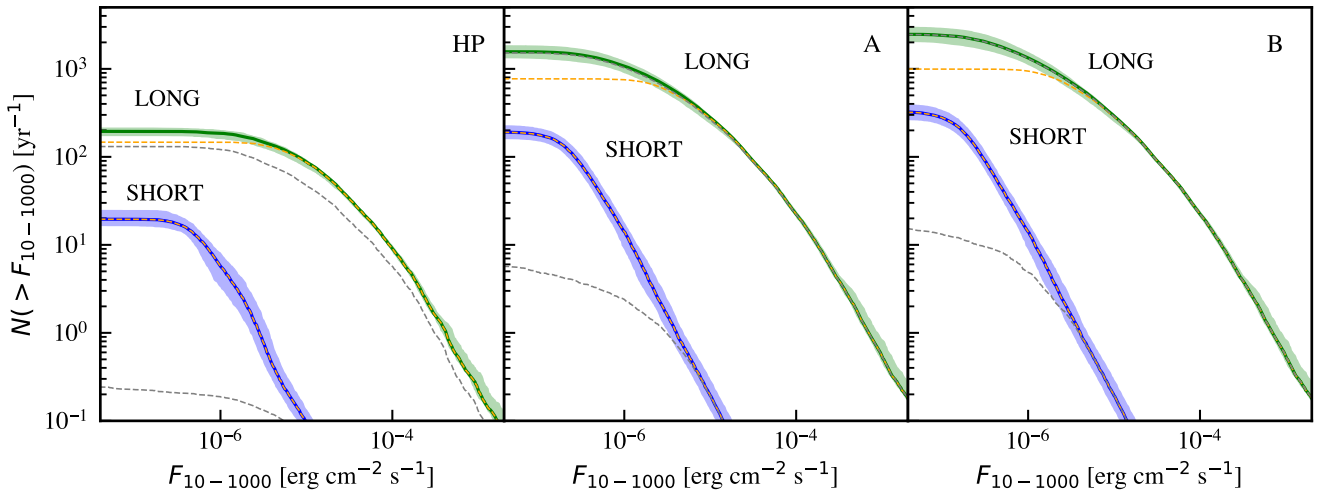
Fig. 4. Cumulative distributions of the photon peak flux (in the energy range 10–1000 keV) for the GRBs detected by HERMES HP (left panel), Constellation A (center), and Constellation B (right). In each panel, the cumulative curve for long (short) GRBs is shown in green (blue), and the shaded region includes 68% of the realisations. Orange (gray) dashed curves show the contribution of the S (X) detection mode. For Constellations A and B, almost all long GRBs are detected by the X mode, making the dashed gray curve almost overlap with the total distribution (solid green curve).

Fig. 5. Cumulative distributions of the fluence (in the energy range 10–1000 keV) for the GRBs detected by HERMES HP (left panel), Constellation A (center), and Constellation B (right). In each panel, the cumulative curve for long (short) GRBs is shown in green (blue), and the shaded region includes 68% of the realisations. Orange (gray) dashed curves show the contribution of the S (X) detection mode.

to the larger FoV of the S instrument. Moving to lower flux and fluence, the fraction of GRBs detected by the X-mode over the total increases. This is due to fainter events also being typically softer (i.e., their peak energy is located at lower energies), owing to the assumption of the $E_{peak}-E_{iso}(L_{iso})$ correlations[5] holding for long GRBs, thus favoring detections with the X-mode (X-only events in Table 2). This effect is clearly visible in Fig. 3, where the location of the HERMES GRBs in the observer frame E_{peak}–peak flux plane is shown and compared to Fermi/GBM GRBs. Blue regions show the GRBs detected by HERMES-Constellation B and green contours mark the subsample of GRBs detected only by the X-mode. Red dashed contours show the GBM GRBs for comparison. Long HERMES GRBs (left-hand panel in Fig. 3) extend to lower peak energies, mostly thanks to the X detection mode, which allows the detection of softer

GRBs compared to the GBM. Our long-GRB population model includes X-ray flashes (XRFs) and X-ray-rich GRBs (XRRs) as a continuous extension of the luminosity function to low values (e.g., based on the result of Pescalli et al. 2015) together with the assumption of the $E_{peak}-E_{iso}$ correlation. Therefore, long GRBs, XRFs, and XRRs are considered to be a unique population. If XRFs and/or XRRs were to have an intrinsic rate exceeding that of "hard" GRBs, the detection rates estimated in this work would increase. Therefore, the soft-energy extension of HERMES detectors down to 4 keV represents an opportunity to explore the nature and rate of XRF and XRR bursts (see Fig. 3). Since short GRBs are, on average, harder than long ones (Ghirlanda et al. 2004), the short GRB population accessible to HERMES is similar to that accessible to the GBM (right-hand panel in Fig. 3).

We note that the $E_{peak}-E_{iso}$ correlation is assumed to hold among long GRBs for the construction (Ghirlanda et al. 2015) of the synthetic population used here. However, there

---

[5] These correlations were implemented with their scatter in the population model; see Ghirlanda et al. (2015).

Table 3. HERMES detection threshold photon flux.

	LONG		SHORT	
	P_{lim}^{50-300} ph cm^{-2} s^{-1}	$P_{\text{lim}}^{10-1000}$ ph cm^{-2} s^{-1}	P_{lim}^{50-300} ph cm^{-2} s^{-1}	$P_{\text{lim}}^{10-1000}$ ph cm^{-2} s^{-1}
HP	0.8	3.1	5.6	12.1
Const. A	0.07	0.41	1.1	2.4
Const. B	0.02	0.15	0.74	1.6

Notes. For long and short GRBs the detection threshold photon flux is computed at 1 s and 64 ms, respectively. Threshold value is calculated as the photon flux above which at least 80% of the GRBs falling within the FoV are actually detected at more than 5σ. For each single module of the HP and of the Constellations A and B, the FoV is reported in Table 1.

are two outliers of this correlation, namely GRB980425 and GRB031203 (but see Ghisellini et al. 2006), which might be representative of a larger number of similar events (Heussaff et al. 2013). These appear as relatively low-luminosity bursts ($\sim 10^{47-48}$ erg s^{-1}) with large intrinsic peak energies (in the range 100–250 keV). The observed fluence of GRB980425 is $\sim 3 \times 10^{-6}$ erg cm^{-2}, which would make it detectable by HERMES Constellations A and B (mid and right panels of Fig. 5) while being at the limit of the performances of HP. The intrinsic rate density of 980425-like low-luminosity events is $\rho_{LL} \sim 230^{+490}_{-190}$ Gpc^{-3} yr^{-1} (Soderberg et al. 2006; Pescalli et al. 2015). By computing the maximum distance out to which a GRB980145-like event would be detectable with a significance of $>5\sigma$ by HERMES, we estimate that HERMES Pathfinder would detect a GRB980425-like event every ~ 5 years. HERMES Constellation A (B) would be able to catch approximately five (ten) such events per year owing to its higher sensitivity and full sky coverage.

To quantify a representative detection threshold of HERMES Pathfinder for long and short GRBs, we estimated for which limiting values of the peak flux the fraction of detected events is $\geq 80\%$ of the total simulated events (falling within the FoV). This value is reported in Table 3.

4. Detection of short GRBs as gravitational-wave counterparts

The first and still unique event with an associated electromagnetic (EM) counterpart, GW170817 (Abbott et al. 2017b), marked the beginning of the MM era. Produced by the merger of two neutron stars, this event was associated with the short GRB 170817A (Abbott et al. 2017b) and, thanks to intensive worldwide multiwavelength follow-up efforts, with the optical near-infrared transient AT2017gfo (Coulter et al. 2017), spectroscopically classified (e.g. Pian et al. 2017) as a kilonova (KN, Li & Paczyński 1998; Metzger 2019). The study of the thermal (KN) and nonthermal (short-GRB and afterglow) emission of GW170817 provided us with unique clues as to the dynamics and ejecta properties resulting from a BNS merger, the formation site of heavy elements, and the progenitor of short GRBs (see e.g., Nakar & Piran 2021; Margutti & Chornock 2021).

GRBs are narrowly collimated sources (e.g., Frail et al. 2001) with highly relativistic outflows, such that their brightness, and consequently their detection probability, depend on the orientation of their jets in the plane of the sky, that is, in addition to their luminosity and distance. Therefore, EM detectors, given their limiting sensitivity, introduce an instrumental selection bias on the jet orientation, with more aligned jets being detected at larger distances. Similarly, the GW signal intensity depends on

the orientation of the binary orbital plane with respect to the line of sight, in addition to the source distance: face-on events (with their orbital plane perpendicular to the line of sight) are detectable by GW interferometers at larger distances (setting the GW network horizon). Based on arguments related to symmetry, the GRB jet axis is expected to be perpendicular to the binary orbital plane, and hence the GW and GRB brightness are correlated.

The current GW detector network can detect BNS mergers out to a few hundred megaparsecs. Based on present BNS detections, the inferred local rate density of BNS mergers is between 10 and 1700 events per Gpc^3 per yr (Abbott et al. 2023 union of 90% credible intervals from different methods). In the fourth LVK observing run (O4, started in May 2023), despite the expected rate of ten GW detections per year by BNS, only up to one joint GW–GRB detection is envisaged (Colombo et al. 2022). Such a small rate is mainly due to the limited GW horizon, within which, given the small rate density of SGRBs, detected events will be dominated by jets seen off-axis. In turn, these would be too faint for the current GRB detector performances.

Third-generation gravitational wave interferometers such as the ET, expected to be operational in 2035 (Maggiore et al. 2020), will extend the GW horizon out to several gigaparsecs, thus including the full BNS cosmic population up to and beyond the redshift of the peak of the BNS merger rate density. ET will detect $\mathcal{O}(5)$ BNS mergers per year, of which a considerable number $\mathcal{O}(1-2)$ will be sufficiently bright to be jointly detected in γ-rays by future space-based missions as prompt short GRBs (Ronchini et al. 2022).

We estimated the joint GW–EM detection rates adopting the same structured-jet short-GRB population as in the previous sections (Salafia et al. 2023). We assumed all short GRBs to be produced in the aftermath of a BNS merger. Hence, we considered only the population model hyperparameter values[6] that yield a local rate density of SGRBs (including all viewing angles) that is consistent with the uncertainty range 10–1700 Gpc^{-3} yr^{-1} estimated for BNS mergers from the GWTC-3 catalog population analysis (Abbott et al. 2023).

Given the expected evolution of the HERMES project, we considered HP for the prediction of the joint GW plus GRB detection rates expected during the fifth observing run (O5) of the current ground-based GW detector network (we considered LIGO Handford, LIGO Livingston, and Virgo, namely a "HLV" network). For predictions relevant to the era of next-generation ground-based GW detectors, we considered HER-

---

[6] We used the hyper-posterior samples for the fiducial "full-sample analysis" in Salafia et al. (2023), publicly available at https://doi.org/10.5281/zenodo.8160783

MES Constellations A and B and took the ET single-triangle 10 km arm configuration as the representative GW detector.

In order to estimate the GW detection rates, we considered a chirp mass of $M_{chirp} = 1.18 \, M_\odot$ (similar to GW170817) for all BNSs, and we adopted the ET-D sensitivity curve (ET Collaboration 2009) for ET and the projected O5 sensitivity curves (LVK Collaboration 2022) for the HLV network. We assumed 100% duty cycles for simplicity. We computed the signal-to-noise ratio (S/N) in each GW detector using the simple `gwsnr` code[7], employing the quasi-Newtonian inspiral frequency-domain waveform from Maggiore (2018), with a cutoff at the innermost stable circular orbit frequency. We considered a detection whenever the network signal-to-noise ratio S/N_{net} (i.e., the sum square of the S/N of each detector in the network) exceeded $S/N_{net} > 12$. The capability of HERMES to detect the GRB counterpart was modeled as described in the previous sections.

The resulting cumulative detection rates are shown in Fig. 6. The top panels refer to O5, while the bottom panels refer to the ET era. The left-hand panels show cumulative detection rates within redshift z, while the right-hand panels show cumulative detection rates for viewing angles of larger than θ_v. The latter is defined as the angle between the GRB jet axis (assumed to be perpendicular to the binary orbital plane) and the line of sight. In each panel, the full population (as observed with a hypothetical infinitely sensitive detector) is shown in light gray, while other colors refer to detection by HERMES (red), the GW detector network (purple for the HLV network, cyan for ET), or both (green). The shaded band around each line encompasses the 90% credible range of the corresponding rate, as derived from the posterior probability on the hyperparameters of the Salafia et al. (2023) model.

Table 4 reports the joint detection rates, including the less likely configurations of HERMES HP together with ET, which would imply an unsuccessful upgrade of the detector sensitivity over the next decade, and the combination of Constellations A and B with O5, which would instead imply a very fast development of the Constellations.

5. Discussion and conclusions

We computed the rates of long and short GRBs detectable by HERMES. We considered the HERMES Pathfinder instrument setup and two possible improved configurations, namely the HERMES Constellations (see Table 1 and Fig. 1). Here, we accounted for the effective area boresight angle dependence and for the sky coverage of the possible HERMES configurations, adopting state-of-the-art population models for short and long GRBs.

We find that (Table 2) ~195 (~19) yr^{-1} long (short) GRBs should be detected by the HERMES Pathfinder (about 80 long GRBs and 8 short GRBs per year should be detected by SpIRIT). This assumes an observation efficiency of 50%, which is appropriate for the SSO of SpIRIT, which is smaller than the 75–80% achievable on equatorial LEO orbits.

A substantial increase in the detection rates of long and short GRBs (Table 2) is expected for HERMES Constellations (configurations A or B), which assumes a four-times-larger effective area and nine CubeSats (Constellation A) and a possible reduction in the background (through a reduced FoV for the single CubeSat but a larger number of 13 units – Constellation B). Intriguingly, we estimate that ~40–70 long GRBs per year at

redshift $z > 6$ can be detected by the HERMES Constellation thanks to its energy extension down to the soft X-rays. Considering the present sample of eight GRBs known at $z > 6$, which have been collected over the last two decades, HERMES Pathfinder, with 3.4 yr^{-1} at $z > 6$, could already help double this sample in a couple of years, if NIR follow up of these events is secured by ground-based facilities. One of the major hurdles to be overcome in order to achieve this goal is the precise localization of the burst. Localizations obtained with the triangulation technique are limited by three main factors: (1) the projected baseline, (2) the temporal structure of the GRB, and (3) the GRB brightness (see e.g., Sanna et al. 2020; Thomas et al. 2023; Burgess et al. 2018). HP and SpIRIT use a low-Earth orbit, implying a maximum projected baseline of ≲10 000–12 000 km. With a projected baseline of the order of 7000 km, we predict that HP will provide the capability to constrain at least one coordinate of bright bursts with temporal structure down to a few milliseconds, with an accuracy ranging from a few tenths to several tens of degrees. The cause of poor sensitivity in one coordinate originates from the geometrical limitation due to the fact that the six HP units will fly on the same orbital plane. Constellations A and B would use at least two different orbital planes, allowing similar constraints on both GRB coordinates. Localization accuracy will be significantly better than that achievable by HP thanks to the larger collecting area and the higher number of satellites. The localization accuracy of faint bursts with smooth temporal structure will in any case be limited using the triangulation technique with satellites in low Earth orbit (LEO). However, the localization capabilities can be improved by complementing the triangulation technique with other techniques, such as the counts aspect ratio technique, which has been used, for example, by the Fermi/GBM instrument, and by increasing the projected baseline. To the latter purpose, future constellations based on the HP concept (low cost, fast track) would greatly benefit from the infrastructure that is being setup around the Moon in the context of the Artemis program. Relay communications, navigation services, and accurate real-time positioning are all goals of the ESA Moonlight initiative[8], which would enable the deployment of segments of GRB-dedicated constellations around the Moon, thus improving localization capabilities by a factor ~50.

We estimated the expected contribution of HERMES to the detection of the prompt emission of short GRBs as EM counterparts of GW events due to BNS mergers. These results are shown in Fig. 6 and reported in Table 4. First of all, both during O5 and in the ET era, the short-GRB detection horizon is set by the GW detector rather than HERMES: the latter can efficiently detect events almost out to $z \sim 3$, while the HLV network is limited to $z \lesssim 0.2$ and ET to $z \lesssim 2$. According to this population model (which predicts a strong event density evolution with redshift; see Salafia et al. 2023), the total rate of BNS mergers in the Universe is very large, $\dot{N}_{BNS,tot} = 9.2^{+58}_{-7.4} \times 10^6$ yr^{-1}. The HLV network can detect around 1 in 10^5 of these events, with a total predicted detection rate in O5 of $\dot{N}_{obs,HLV} = 70^{178}_{-57}$ yr^{-1}. Only a small fraction of these events is detected in conjunction with HERMES HP, $\dot{N}_{obs,HP+HLV} = 1.0 \pm 0.5$ yr^{-1}. The right-hand panels show that while the typical viewing angle of jets that produce an EM-detectable GRB is around a few degrees, the joint GW+GRB events have a larger typical viewing angle of several degrees.

The multimessenger prospects significantly improve in the third-generation GW detector era: ET can detect more than 1% of the total population, amounting to $\dot{N}_{obs,ET} = 1.9^{+5.4}_{-1.6} \times 10^5$ yr^{-1}.

---

[7] https://github.com/omsharansalafia/gwsnr

[8] https://www.esa.int/Applications/Connectivity_and_Secure_Communications/Moonlight
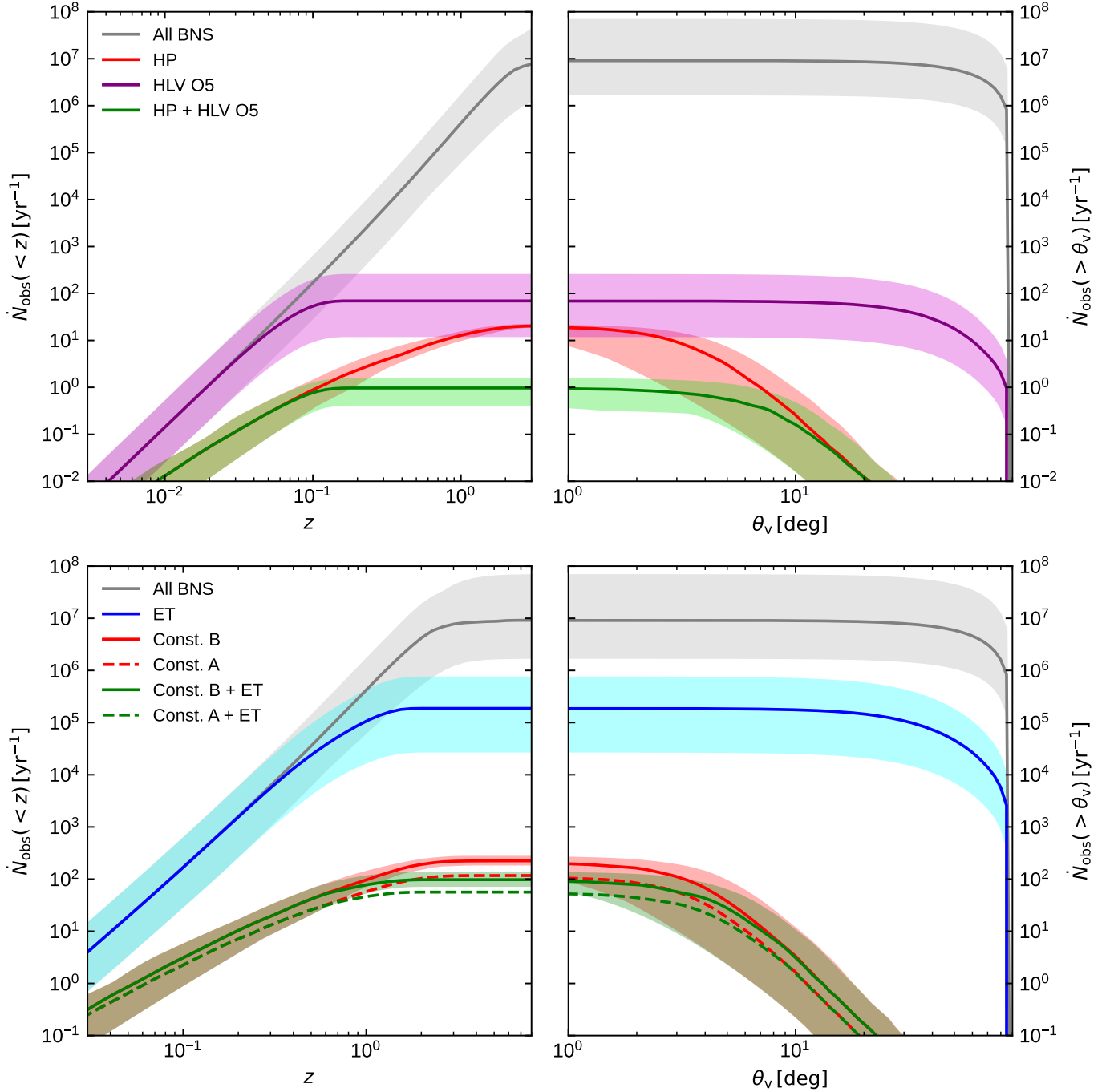
Fig. 6. Top-left panel: Cumulative detection rates as a function of redshift at the time of the O5 GW detector network run. Different colors refer to subpopulations that satisfy different detection cut combinations (gray: all events; purple: detection by the HLV GW network with O5 sensitivity; red: detection by HERMES Pathfinder; green: joint detection by HERMES and the HLV network). For each subpopulation, the solid line shows the median cumulative rate, while the shaded band encompasses the 90% credible range at fixed z. Top-right panel: Inverse-cumulative rates of events with a viewing angle larger than a given threshold. The meaning of the colors, lines, and bands is the same as in the top-left panel. Bottom-left panel: Similar to the top-left panel, but for HERMES constellations A and B, together with the ET GW detector at design sensitivity (ET-D). Light blue refers to the ET cumulative detection rate; the red solid line and shaded region show the detection rate (median and 90% uncertainty) by the HERMES Constellation B, while the red dashed line shows the median for Constellation A. The green solid line and green shaded region refer to events detected by both ET and HERMES Constellation B. The dashed line shows the median detection rate for ET and HERMES Constellation A. Bottom-right panel: Similar to the top-right panel, but for ET and HERMES Constellations A and B.

Thanks also to the improved HERMES Constellation sensitivity, the joint GW+GRB detection rates are also much more encouraging: for Constellation A, we predict $\dot{N}_{\mathrm{obs,A+ET}} = 56^{+7}_{-12}$ yr^{-1}, while for Constellation B the joint detection rate increases to $\dot{N}_{\mathrm{obs,B+ET}} = 97^{+36}_{-23}$ yr^{-1}. The typical viewing angle of BNS mergers observed as a multimessenger source in the ET era, on the other hand, is closer to that of EM-only events: this is because the GRB brightness decreases quickly with the viewing angle (Salafia et al. 2023) and therefore the increased joint detection rate follows mainly from the improved GW horizon, while the

Table 4. Joint GW–EM detection rates.

	HP	Const. A	Const. B
O5	$0.97^{+0.54}_{-0.54}$	$2.5^{+1.8}_{-1.7}$	$3.5^{+2.7}_{-2.4}$
ET	12^{+2}_{-2}	56^{+7}_{-12}	97^{+36}_{-23}

Notes. Number of events per year of GW BNS events detected during HLV O5 and by the *Einstein* Telescope with their prompt jet emission (GRB) detected by HERMES.

improved GRB sensitivity of the HERMES Constellations does not push the limiting viewing angle to much larger values.

References

Abbott, B. P., Abbott, R., Abbott, T. D., et al. 2017a, Class. Quant. Grav., 34, 044001

Abbott, B. P., Abbott, R., Abbott, T. D., et al. 2017b, ApJ, 848, L13

Abbott, R., Abbott, T. D., Acernese, F., et al. 2023, Phys. Rev. X, 13, 011048

Acernese, F., Agathos, M., Agatsuma, K., et al. 2015, Class. Quant. Grav., 32, 024001

Agostinelli, S., Allison, J., Amako, K., et al. 2003, Nucl. Instrum. Methods Phys. Res. A, 506, 250

Akutsu, T., Ando, M., Arai, K., et al. 2020, Prog. Theor. Exp. Phys., 2021, 05A101

Amati, L., O'Brien, P. T., Götz, D., et al. 2021, Exp. Astron., 52, 183

Atteia, J. L., Cordier, B., & Wei, J. 2022, IJMPD, 31, 2230008

Bélanger, G. 2013, ApJ, 773, 66

Bernardini, M. G., Bissaldi, E., Bosnjak, Z., et al. 2019, Int. Cosm. Ray Conf., 36, 598

Branchesi, M., Maggiore, M., Alonso, D., et al. 2023, JCAP, 2023, 068

Bromberg, O., Nakar, E., Piran, T., & Sari, R. 2013, ApJ, 764, 179

Burgess, J. M., Yu, H.-F., Greiner, J., & Mortlock, D. J. 2018, MNRAS, 476, 1427

Campana, R., Feroci, M., Del Monte, E., et al. 2013, Exp. Astron., 36, 451

Campana, R., Fuschino, F., Evangelista, Y., Dilillo, G., & Fiore, F. 2020, SPIE Conf. Ser., 11444, 114444U

Campana, R., Baroni, G., Della Casa, G., et al. 2022, SPIE Conf. Ser., 12181, 121815K

Chandra, P., & Frail, D. A. 2012, ApJ, 746, 156

Colagrossi, A., Prinetto, J., Silvestrini, S., et al. 2019, Proceedings of the 70th International Astronautical Congress (IAC 2019), Washington D.C., 21–25 October 2019, 1

Colagrossi, A., Prinetto, J., Silvestrini, S., & Lavagna, M. 2020, J. Astron. Telesc. Instrum. Syst., 6, 048001

Colombo, A., Salafia, O. S., Gabrielli, F., et al. 2022, ApJ, 937, 79

Colombo, A., Duqué, R., Sharan Salafia, O., et al. 2024, A&A, 686, A265

Coulter, D. A., Foley, R. J., Kilpatrick, C. D., et al. 2017, Science, 358, 1556

Crupi, R., Dilillo, G., Bissaldi, E., et al. 2023, Exp. Astron., 56, 421

Dilillo, G., Ward, K., Eckley, I. A., et al. 2024, ApJ, 962, 137

Eichler, D., Livio, M., Piran, T., & Schramm, D. N. 1989, Nature, 340, 126

ET Collaboration 2009, ET sensitivities page, https://www.et-gw.eu/index.php/etsensitivities

Evangelista, Y., Fiore, F., Fuschino, F., et al. 2020, SPIE Conf. Ser., 11444, 114441T

Evangelista, Y., Fiore, F., Campana, R., et al. 2022, SPIE Conf. Ser., 12181, 121811G

Fiore, F., Burderi, L., Lavagna, M., et al. 2020, SPIE Conf. Ser., 11444, 114441R

Fiore, F., Werner, N., & Behar, E. 2021, Galaxies, 9, 120

Fiore, F., Guzman, A., Campana, R., & Evangelista, Y. 2022, in Handbook of X-ray and Gamma-ray Astrophysics, eds. C. Bambi, & A. Santangelo (Springer Living Reference Work), 38

Frail, D. A., Kulkarni, S. R., Sari, R., et al. 2001, ApJ, 562, L55

Gehrels, N., Chincarini, G., Giommi, P., et al. 2004, ApJ, 611, 1005

Ghirlanda, G., Ghisellini, G., & Celotti, A. 2004, A&A, 422, L55

Ghirlanda, G., Nava, L., Ghisellini, G., Celotti, A., & Firmani, C. 2009, A&A, 496, 585

Ghirlanda, G., Salvaterra, R., Burlon, D., et al. 2013, MNRAS, 435, 2543

Ghirlanda, G., Burlon, D., Ghisellini, G., et al. 2014, PASA, 31, e022

Ghirlanda, G., Salvaterra, R., Ghisellini, G., et al. 2015, MNRAS, 448, 2514

Ghirlanda, G., Salafia, O. S., Paragi, Z., et al. 2019, Science, 363, 968

Ghisellini, G., Ghirlanda, G., Mereghetti, S., et al. 2006, MNRAS, 372, 1699

Giarratana, S., Rhodes, L., Marcote, B., et al. 2022, A&A, 664, A36

Golkhou, V. Z., Butler, N. R., & Littlejohns, O. M. 2015, ApJ, 811, 93

Granja, C., Hudec, R., Maršíková, V., et al. 2022, Universe, 8, 241

Guzman, A., Pliego, S., Bayer, J., et al. 2020, SPIE Conf. Ser., 11444, 1144450

H.E.S.S. Collaboration (Abdalla, H., et al.) 2021, Science, 372, 1081

Heussaff, V., Atteia, J. L., & Zolnierowski, Y. 2013, A&A, 557, A100

Huang, Y., Hu, S., Chen, S., et al. 2022, GCN, 32677, 1

Kouveliotou, C., Meegan, C. A., Fishman, G. J., et al. 1993, ApJ, 413, L101

Levan, A., Crowther, P., de Grijs, R., et al. 2016, Space Sci. Rev., 202, 33

Li, L.-X., & Paczyński, B. 1998, ApJ, 507, L59

Lien, A., Sakamoto, T., Gehrels, N., et al. 2014, ApJ, 783, 24

LIGO Scientific Collaboration (Aasi, J., et al.) 2015, Class. Quant. Grav., 32, 074001

LVK Collaboration 2022, Noise Curves for use in simulations pre-O4, https://dcc.ligo.org/T2200043-v3/public

MacLachlan, G. A., Shenoy, A., Sonbas, E., et al. 2013, MNRAS, 432, 857

Maggiore, M. 2018, Gravitational Waves: Volume 2: Astrophysics and Cosmology (Oxford: Oxford University Press)

Maggiore, M., Van Den Broeck, C., Bartolo, N., et al. 2020, JCAP, 2020, 050

MAGIC Collaboration (Acciari, V. A., et al.) 2019, Nature, 575, 459

Margutti, R., & Chornock, R. 2021, ARA&A, 59, 155

Meegan, C., Lichti, G., Bhat, P. N., et al. 2009, ApJ, 702, 791

Metzger, B. D. 2019, Liv. Rev. Relat., 23, 1

Miceli, D., & Nava, L. 2022, Galaxies, 10, 66

Mooley, K. P., Deller, A. T., Gottlieb, O., et al. 2018, Nature, 561, 355

Nakar, E., & Piran, T. 2021, ApJ, 909, 114

Narayan, R., Paczynski, B., & Piran, T. 1992, ApJ, 395, L83

Pál, A., Ohno, M., Mészáros, L., et al. 2020, SPIE Conf. Ser., 11444, 114444V

Pál, A., Ohno, M., Mészáros, L., et al. 2023, A&A, 677, A40

Pescalli, A., Ghirlanda, G., Salafia, O. S., et al. 2015, MNRAS, 447, 1911

Pian, E., D'Avanzo, P., Benetti, S., et al. 2017, Nature, 551, 67

Poolakkil, S., Preece, R., Fletcher, C., et al. 2021, ApJ, 913, 60

Punturo, M., Abernathy, M., Acernese, F., et al. 2010, Class. Quant. Grav., 27, 194002

Rastinejad, J. C., Gompertz, B. P., Levan, A. J., et al. 2022, Nature, 612, 223

Reitze, D., Adhikari, R. X., Ballmer, S., et al. 2019, BAAS, 51, 35

Řípa, J., Pál, A., Ohno, M., et al. 2022, SPIE Conf. Ser., 12181, 121811K

Ronchini, S., Branchesi, M., Oganesyan, G., et al. 2022, A&A, 665, A97

Rossi, A., Rothberg, B., Palazzi, E., et al. 2022, ApJ, 932, 1

Salafia, O. S., & Ghirlanda, G. 2022, Galaxies, 10, 93

Salafia, O. S., Ravasio, M. E., Yang, J., et al. 2022, ApJ, 931, L19

Salafia, O. S., Ravasio, M. E., Ghirlanda, G., & Mandel, I. 2023, A&A, 680, A45

Sanna, A., Burderi, L., Di Salvo, T., et al. 2020, SPIE Conf. Ser., 11444, 114444X

Soderberg, A. M., Kulkarni, S. R., Nakar, E., et al. 2006, Nature, 442, 1014

Thomas, M., Trenti, M., Sanna, A., et al. 2023, PASA, 40, e008

Trenti, M. 2021, 43rd COSPAR Scientific Assembly. Held 28 January – 4 February, 43, 1507

Ward, K., Dilillo, G., Eckley, I., & Fearnhead, P. 2023, J. Am. Stat. Assoc., 1 https://doi.org/10.1080/01621459.2023.2235059

White, N. E., Bauer, F. E., Baumgartner, W., et al. 2021, SPIE Conf. Ser., 11821, 1182109

Woosley, S. E. 1993, ApJ, 405, 273

Yuan, W., Zhang, C., Chen, Y., & Ling, Z. 2022, in Handbook of X-ray and Gamma-ray Astrophysics, eds. C. Bambi, & A. Santangelo (Springer Living Reference Work), 86

---

[1] INAF – Osservatorio Astronomico di Brera, via E. Bianchi 46, I-23807 Merate (LC), Italy

[2] INFN – Sezione di Milano-Bicocca, piazza della Scienza 3, I-20126 Milano, Italy

[3] INAF – Osservatorio Astronomico di Trieste, Via G.B. Tiepolo 11, I-34143 Trieste, Italy

[4] IFPU – Institut for Fundamental Physics of the Universe, Via Beirut 2, I-34014 Trieste, Italy

[5] INAF – OAS, Via Piero Gobetti 101, Bologna I-40129, Italy

[6] INFN – Sezione di Bologna, Viale Berti Pichat 6/2, Bologna I-40127, Italy

[7] INAF – Istituto di Astrofisica Spaziale e Fisica Cosmica di Milano, Via A. Corti 12, 20133 Milano, Italy

[8] Dipartimento di Fisica, Università degli Studi di Cagliari, SP Monserrato–Sestu km 0.7, 09042 Monserrato, Italy

[9] Dipartimento di Fisica, Università di Trento, Sommarive 14, 38122 Povo (TN), Italy

[10] INAF – Istituto di Astrofisica e Planetologia Spaziali, Via del Fosso del Cavaliere 100, I-00133 Roma (RM), Italy

[11] INFN – Sezione di Roma Tor Vergata, Via della Ricerca Scientifica 1, I-00133 Roma (RM), Italy

[12] Agenzia Spaziale Italiana, Via del Politecnico snc, 00133 Roma, Italy

[13] Institut für Astronomie und Astrophysik, Universität Tübingen, Sand 1, D-72076 Tübingen, Germany

[14] School of Physics, University of Melbourne, Parkville Vic 3010, Australia

[15] Australian Research Council Centre of Excellence for All-Sky Astrophysics in 3-Dimensions, Stromlo, Australian Capital Territory

[16] Physics Department, Federico II University, via Cintia 21, I-80126 Napoli, Italy

[17] Politecnico di Milano - Department of Aerospace Science and Technology, Milan, Italy

[18] Fondazione Bruno Kessler, Center for Sensors and Devices, Trento, Italy

[19] Politecnico di Milano - Department of Electronics, Information and Bioengineering, Como, Italy

[20] Dipartimento di Matematica e Informatica, Università degli Studi di Cagliari, SP Monserrato–Sestu km 0.7, 09042 Monserrato, Italy

[21] Key Laboratory of Particle Astrophysics, Institute of High Energy Physics, Chinese Academy of Sciences, Beijing 100049, China

[22] INAF - IASF Palermo, Via Ugo La Malfa 153, 90146 Palermo, Italy

[23] Dipartimento di Fisica e Chimica, Università degli Studi di Palermo, via Archirafi 36, I-90123 Palermo, Italy

[24] SkyLabs d.o.o., Zagrebška c. 104, 2000 Maribor, Slovenia

[25] Center for Astrophysics and Cosmology, University of Nova Gorica, Vipavska 13, 5000 Nova Gorica, Slovenia

[26] Department of Electrical, Computer and Biomedical Engineering, University of Pavia, Pavia I-27100, Italy

[27] Department of Theoretical Physics and Astrophysics, Faculty of Science, Masaryk University, Brno, Czech Republic

[28] INAF – Osservatorio Astronomico di Roma, Via Frascati 33, I-00078 Monte Porzio Catone (RM), Italy

[29] Department of Mathematical, Informatics, and Physics University of Udine, Udine I-33100, Italy

[30] INAF - OAPA, piazza del Parlamento 1, 90134 Palermo, Italy